Politecnico di Torino

Politecnico di Torino

Corso di Laurea Magistrale in Ingegneria Aerospaziale

A.a. 2020/2021

Sessione di Laurea Dicembre 2021

Implementation and investigation of subgrid-scale models in particle-laden flows

Relatore:

Prof. Francesco Larocca

Candidato:

Antonino Tudisca

Relatori esterni:

Prof. Stephan Staudacher

M.Sc. Patrick Kopper

M.Sc. Anna Schwarz

Master thesis

Implementation and investigation of subgrid-scale models in particle-laden flows

Herr cand. aer. Antonino Tudisca

October 2021

Nr. 1560

Institut für Luftfahrtantriebe
Universität Stuttgart
Direktor: Prof. Dr.-Ing. S. Staudacher

Abstract

The master thesis project concerns the particles behaviour in a turbulent multiphase flow and it was conducted at the Institute of Aircraft Propulsion Systems (ILA) of the University of Stuttgart. To perform Large-eddy simulations (LES) of particle-laden flows the open-source solver FLEXI developed at the Institute of Aerodynamics and Gas Dynamics (IAG) is used. In the context of LES, subgrid-scale (SGS) models are required in order to approximate the unresolved scales of the fluid phase on the particle motion. To investigate the particle behaviour the two SGS models of Sommerfeld [17] and Minier et al. [17] are implemented and validated in FLEXI. Therefore, the model of Breuer et al. [6], previously implemented, is used as well. The performance of these models are evaluated through simulations of a particle-laden flow in a round-jet. First, the numerical results are compared against the experimental data of Fan et al. [8]. It was found that due small differences in the setting of the simulations the numerical results are and characterised by a higher spreading of the particles and smaller turbulent kinetic energy. Second, to further evaluate the performance the SGS results are compared with the simulation in which no SGS model is employed. In the end only minor differences are visible between the simulations, in which all the quantities analysed for each SGS model are characterised by the same trend.

Keywords: Large-eddy simulations (LES), subgrid-scale (SGS), particles, turbulent kinetic energy, particle-laden flow, round-jet, turbulent multiphase flow

Contents

List of Figures

List of Tables

Nomenclature

General convection

- The scalar quantities are represented in lowercase italics (a), the vectors in italics and bold ($\boldsymbol{b}$).
- Second-order tensors in upper-case, italics and boldface ($\boldsymbol{C}$).

Latin Letter

Name	**Unit**	**Description**
b	–	Csanady's factor
d	m	Diameter
dt	s	Timestep
e	J/kg	Specific total energy
f	N	Force acting on the particles
g	m/s^2	Gravity acceleration
k	m^2/s^2	Kinetic energy
L	s	Eulerian timescale
m	kg	Mass
p	Pa	Pressure
q	W/m^2	Molecular heat
r	–	Nodal point
R	$J/kg \cdot K$	Specific gas constant
Re	–	Reynolds number
St	–	Stokes number
T	s	Integral timescale, temperature in Navier-Stokes equations
u	m/s	Instantaneous velocities in x,y,z direction

$\overline{u}$	m/s	Filtered velocity
x,y,z	m	Position, direction

Greek Letters

Name	Einheit	Beschreibung
β	–	Ratio Integral/Eulerian timescale
δ	–	Kronecker delta
Δ	m	Grid length
γ	–	Air constant
ϵ	m^2/s^3	Energy dissipation rate
ζ	–	Computation space
μ	$Pa \cdot s$	Dynamic viscosity
ν	m^2/s	Kinematic viscosity
ρ	kg/m^3	Density
σ	m/s	Standard deviation
τ_p	s	Particle relaxation time

Superscript

$(\,)'$	Fluctuation term

Subscript

$(\,)_0$	Initial condition
$(\,)_{\|\|}$	Parallel direction
$(\,)_\perp$	Perpendicular direction
$(\,)_\mathrm{E}$	Eulerian
$(\,)_\mathrm{f}$	Fluid
$(\,)_i$	Directions (i=1,2,3)
$(\,)_{ij}$	Matrix indices
$(\,)_\mathrm{L}$	Lagrangian
$(\,)_\mathrm{r}$	Relative
$(\,)_\mathrm{p}$	Particle

$(\,)_{\mathrm{SGS}}$	Subgrid-scale

Abbreviations

ADM	Approximate Deconvolution models
DGSEM	Discontinuous Galerkin spectral element method
DNS	Direct numerical simulation
LES	Largy-eddy simulation
PDF	Probability Density Function
RANS	Reynolds-averaging Navier-Stokes
RHS	Right-hand-side
rms	Root mean square
SDE	Stochastic Differential Equation
SGS	Subgrid-scale
TKE	Turbulent kinetic energy

1 Introduction

The particle behaviour has an important influence in a turbulent multiphase flow and involves several natural process and engineering applications, e.g. dispersion of solid particles in gas or in a liquid. Some examples of this are the burning of solid or liquid fuels in a combustion chamber, furnaces, the dispersion of pollutants from stacks, and transport of sediments. The difficulty to solve these problems numerically lies in the fact that the physics of these flows is characterised by different time and length scales.

The first aim of the present work is to simulate a turbulent particle-laden flow numerically and then evaluate the performance of the subgrid-scale (SGS) model. The goal of this is to model the influence of the unresolved subgrid-scales of the fluid on the particle motion. In this work, the Euler-Lagrangian approach is used to solve the turbulent multiphase flows. With this approach, the fluid is treated by solving the Navier-Stokes equations in Large-eddy simulation (LES), while particles are tracked individually by solving the equation of motion. Therefore, in the present study, only the fluid-particle interactions (one-way coupling) are taken into account, whereas the particle-fluid and particle-particle interactions (two-way and four-way coupling, respectively) are neglected.

The software used for the simulations is FLEXI [12], a solver, developed at the University of Stuttgart, for hyperbolic/parabolic systems based on the Discontinuous Galerkin spectral element method (DGSEM).

The subgrid-scale models used in this work are the models of Sommerfled [17], Minier et al. [17] and Breuer et al. [6]. The first two models are implemented and validated in FLEXI, while the Breuer et al. [6] model was previously implemented and validated. A round-jet flow is simulated to evaluate the performance of the SGS models. The choice of the round-jet such as a test case rather than, for instance, an isotropic box is justified by the anisotropic characteristics of the test case, in which there is no preferential direction of the spreading of the flow from the nozzle, i.e. pressure gradients in every direction that lead particles to move everywhere depending on their inertia.

The results obtained from these three models are compared with the simulation without SGS model and with the experimental results Fan et al. (1997) [8] in order to analyse the influence of the SGS models. First, three different quantities (particle axial velocity, particle turbulent

kinetic energy and radial concentration) are examined to compare the numerical simulation with the experiment. Then, further comparisons between the SGS models are analysed to better evaluate their performance.

2 Theory

The turbulent flow is a fluid motion characterized by irregular fluctuations, mixing and chaotic changes of pressure and flow velocity. This flow is governed by the inertia forces that are greater than the viscous ones. To predict if the flow is turbulent, the dimensionless Reynolds number ($Re = \rho u L/\mu$) is used, in which ρ is the fluid density, u the velocity, μ the dynamic viscosity and L the characteristic length. It is defined as the ratio between the inertia and the viscous forces, so at low Reynolds number the flow is laminar, while at high Reynolds number the flow is turbulent.
The properties of turbulent flow lead to a wide range of time and length scales in which there are eddies of different sizes. The largest eddy arises from the extraction of energy from the mean flow. In turn, by further transfer of energy the eddies become smaller with a theory called *energy cascade*, in which the energy is transferred with neither production nor dissipation. At the scale of the smallest eddies (Kolmogorov length), the dissipation of kinetic energy occurs due to viscosity (conversion of turbulent kinetic energy into internal energy).
The numerical investigation of turbulent flow is very difficult due to these phenomena and it requires the simulation of the continuous phase as well as the description of the particulate phase. Several approaches to this are available in literature and one of the most popular is the Euler–Lagrange approach. In the present study, this approach is employed. First, the fluid is treated in an Eulerian way by solving the compressible form of the Navier–Stokes equations. Second, the particles are tracked individually through the fluid carrier phase by solving the appropriate equations of motion for each particle.

2.1 Continuous phase

The Navier–Stokes equations can be solved in three ways, with different levels of complexity and accuracy; the difference lies on the degree of modeling. The first way is the Reynolds-averaging Navier-Stokes (RANS) method based on an averaging process of the equations with low computational cost. With this method, all the turbulence effect has to be modeled, which affects the accuracy of the results for the flow field prediction. The second method is direct

numerical simulations (DNS), where the accuracy of the prediction is at its highest. In this approach, the computational cost is high because no model is applied in order to calculate the unresolved scales. Between these two approaches, a commonly used method is (LES) in which the larger scales of the flow are resolved, while the smaller scales are modeled or implicitly solved. If the smaller scales are modeled with an eddy-viscosity model, the type of LES is *explicit*. Instead, in case of *implicit* LES, the length scales of the fluid are resolved up to a certain length-scale Δ, and the scales smaller than Δ are the unresolved ones, i.e. filtered by the grid. Implicit LES is the approach used to solve the Navier–Stokes.
The governing equations that describe the fluid flow are the three-dimensional Navier–Stokes equations, mass and energy conservation. The compressible form of these equations for the conservative variable $\boldsymbol{u}$ are as follows:

$$\boldsymbol{u}_t + \nabla \cdot \Big(\boldsymbol{F_c}(\boldsymbol{u}) - \boldsymbol{F_v}(\boldsymbol{u}, \nabla \boldsymbol{u}) \Big) = 0, \tag{2.1}$$

$$\boldsymbol{u} = \begin{pmatrix} \rho \\ \rho u \\ \rho v \\ \rho w \\ \rho e \end{pmatrix}, \qquad \boldsymbol{f}_{c,i}(\boldsymbol{u}) = \begin{pmatrix} \rho u_i \\ p\delta_{1i} + u_i \rho u \\ p\delta_{2i} + u_i \rho v \\ p\delta_{3i} + u_i \rho w \\ (p + \rho e) u_i \end{pmatrix}, \tag{2.2}$$

$$\boldsymbol{f}_{v,i}(\boldsymbol{u}, \nabla \boldsymbol{u}) = \begin{pmatrix} 0 \\ \mu(\nabla u_1 + \nabla_1 u_i - 2/3 \delta_{1i} \nabla \cdot u) \\ \mu(\nabla u_2 + \nabla_2 u_i - 2/3 \delta_{2i} \nabla \cdot v) \\ \mu(\nabla u_3 + \nabla_3 u_i - 2/3 \delta_{3i} \nabla \cdot w) \\ \sum_{j=1}^{3} [\mu(\nabla u_i + \nabla_i u_j - 2/3 \delta_{ij} \nabla \cdot u_i) u_j] - q_i \end{pmatrix}, \quad i = 1,2,3. \tag{2.3}$$

In these equations $(\cdot)_t$ is the temporal derivative, ρ is the fluid density, u, v and w are the velocities in the three directions x, y, and z, e is the the specific total energy and $(f)_{c,i}$ and $(f)_{v,i}$ represent the convective and the viscous fluxes, respectively. Therefore, δ_{ij} is the Kronecker delta that is one if $i = j$, otherwise is zero. q represents the molecular heat flux in the three directions given by Fourier's law

$$\boldsymbol{q} = -k \nabla T, \tag{2.4}$$

where k is the thermal conductivity and ∇T is the gradient of the temperature for each direction. From the Navier-stokes equations, we obtain the density, the velocity in every direction and

the temperature. The system is closed by the following equation of state:

$$p = (\gamma - 1)(\rho e - \frac{1}{2}\rho V^2), \tag{2.5}$$

where γ equal to 1.4 is the ratio between the specific heat at constant pressure (c_p) and the specific heat at constant volume (c_v) and V is the sum of the velocities in the three directions.

2.2 FLEXI and DGSEM solver

To calculate the continuous phase, i.e. to solve the compressible form of the Navier–Stokes equations, the high order schemes are an efficient method to numerically solve multiscale problems, such as turbulent flows. In this work the discontinuous Galerkin spectral element method (DGSEM) [16] solver FLEXI [12] is used, which is an open-source simulation framework written in Fortran and developed at the Institute of Aerodynamics and Gas Dynamics (IAG) of the University of Stuttgart. FLEXI is a solver for hyperbolic–parabolic systems of partial differential equations based on the method of lines.
FLEXI is used in order to approximate a general system of conservation equations for the conserved variables $\boldsymbol{u}$ in a domain $\Omega \subseteq \mathbb{R}^3$

$$\frac{\partial \boldsymbol{u}(\boldsymbol{x},t)}{\partial t} + \nabla \cdot \Big(\boldsymbol{f_c}(\boldsymbol{u}) - \boldsymbol{f_v}(\boldsymbol{u},\nabla \boldsymbol{u}) \Big) = 0, \tag{2.6}$$

where $\boldsymbol{f_c}$ and $\boldsymbol{f_v}$ are convective and viscous fluxes, respectively. The domain Ω is subdivided into hexahedral elements and the geometry of the faces of these elements are approximated by tensor products of one-dimensional Lagrange interpolating polynomials up to the degree N

$$l_j(r) = \prod_{i=0, i\neq j}^{N} \frac{r - r_i}{r_j - r_i}, \qquad j = 0,\ldots,N, \tag{2.7}$$

where r_i are the nodal points. The approximation of each solution with polynomials leads to some discontinuities between two faces. In order to solve this problem, the Roe's linearization Riemann solver is used, in which the class of entropy fixes by Harten and Hyman [20] is applied. The DGSEM scheme is not applied to each different element, but on a reference cube. For that reason, each element is mapped, with a transfinite mapping $\boldsymbol{x} = \boldsymbol{\chi}(\boldsymbol{\zeta},t)$, onto the reference unit cube element $E = [-1,1]^3$ on the computational space $\boldsymbol{\zeta} = (\zeta^1,\zeta^2,\zeta^3)^T$. For this purpose, it is necessary to introduce the Jacobian of the mapping $\mathcal{J}$ as the determinant of the Jacobian matrix $\nabla_\zeta \boldsymbol{\chi}$, where ∇_ζ is the Nabla operator in computational coordinates. The conservation laws are formulated in the reference cube as well. If we consider a test function $\phi = \phi(\boldsymbol{\zeta})$ and

integrate the equation (2.6) over the reference cube the following formulation is obtained:

$$\left\langle \mathcal{J}\frac{\partial \boldsymbol{u}(\boldsymbol{x},t)}{\partial t},\phi \right\rangle + \int_{\partial E} \phi(\boldsymbol{\mathcal{F}}\cdot\vec{n})dS - \langle \boldsymbol{\mathcal{F}},\nabla_\zeta \phi\rangle = 0, \tag{2.8}$$

in which $\langle\cdot,\cdot\rangle$ represents the inner product, $\vec{n}$ the outward pointing normal vector and $\boldsymbol{\mathcal{F}}$ is the contravariant fluxes as defined by Krais et al. [16]. The integrals are approximated by a quadrature of Gauss-Legendre, and the integration points where the integrals are evaluated are the same as the interpolations points.
The solution is approximated in the reference element as tensor products of Lagrange polynomials of degree N. For instance, if we consider the conservative variable $\boldsymbol{u}$, the 1-D approximation is given by

$$\boldsymbol{u}(\zeta_1,t) = \sum_{m=0}^{N} \boldsymbol{u_m}(t)\psi_m(\zeta_1), \tag{2.9}$$

where $\boldsymbol{u_m}$ defines the degree of freedom. Therefore, in the last equation, it is possible to derive that $\psi_m = l_m(\zeta_1)$ is the associated basis function, and it is evaluated at the same interpolation point (ζ) of the test function. This is the main property of a Galerkin method, and for that the same interpolation point can be used.

2.3 Dispersed phase

In parallel with the calculation of the continuous phase, the calculation of the particle phase must be performed. A Lagrangian approach is used to track the particles in which the dispersed phase is computed by solving Newton's second law for each particle. The general governing equation for smooth rigid spheres with a diameter d_p in the range of the Kolmogorov scale is given by Maxey and Riley [18]

$$m_p\frac{d\boldsymbol{u_p}}{dt} = \boldsymbol{f}_D + \boldsymbol{f}_G + \boldsymbol{f}_B + \boldsymbol{f}_{AM} + \boldsymbol{f}_{PG} + \boldsymbol{f}_L, \tag{2.10}$$

where m_p is the mass of the particle and $\frac{d\boldsymbol{u_p}}{dt}$ is the particle acceleration given by the derivative of the particle velocity $\boldsymbol{u_p}$. On the right hand side (RHS) of Eq. (2.10) the forces considered are are the drag force $\boldsymbol{f}_D$, the gravity force $\boldsymbol{f}_G$, the buoyancy force $\boldsymbol{f}_B$, the added-mass force $\boldsymbol{f}_{AM}$, the pressure-gradient force $\boldsymbol{f}_{PG}$ and the lift force $\boldsymbol{f}_L$.
Following Vinkovic's idea [25], a simplified equation of motion, Eq. (2.11b), can be used on the assumption that ρ_p/ρ_f, i.e. the density ratio between particle and fluid, is $\geq 10^3$. In that case, the influence of all forces can be neglected except the drag and gravity forces. The behavior of particles in a fluid can be described by the dimensionless number $St = \tau_p u_0/l_0$ (Stokes number),

i.e. the ratio between the particle relaxation time τ_p and the characteristic time of the flow. τ_p is the time a particle requires to react to changes of the fluid surrounding the particle, while u_0 and l_0 are the characteristic velocity and dimension of the flow, respectively.
The equation of motion used in order to track the particles individually was already implemented in FLEXI [3] previously the beginning of this work. It is based on the following equations given by Vinkovic [25]

$$\frac{d\boldsymbol{x_p}(t)}{dt} = \boldsymbol{u_p}(t), \tag{2.11a}$$

$$\frac{d\boldsymbol{u_p}(t)}{dt} = \frac{\boldsymbol{u}(\boldsymbol{x_p}(t),t) - \boldsymbol{u_p}(t)}{\tau_p} f(Re_p) + \boldsymbol{g}, \tag{2.11b}$$

$$\tau_p = \frac{\rho_p d_p^2}{18\rho_f \nu}, \tag{2.12}$$

$$Re_p = \frac{|\boldsymbol{u_p} - \boldsymbol{u}| d_p}{\nu}. \tag{2.13}$$

The left hand side of Eq. (2.11a) is the particle velocity as a derivative of the particle position. On the right hand side of (2.11b) there are Stokes drag (first term) and acceleration due to gravity $\boldsymbol{g}$. In the Stokes drag term act the particle velocity, the fluid velocity at the particle position $\boldsymbol{u}(\boldsymbol{x_p}(t),t)$, the fluid kinematic viscosity ν and the particle relaxation time.
Based on the particle Reynolds number Re_p, the effects of non-linear drag are incorporated in $f(Re_p)$ (Maxey and Riley [18]).

2.3.1 SGS model

In order to solve Eq. (2.11b), one has to know the fluid velocity at particle position $x_p(t)$ at time t. The difficulty lies in the accurate prediction of $\boldsymbol{u}(\boldsymbol{x_p}(t),t)$ in a turbulent flow, because with an implicit LES the Navier-Stoke equations provide only the resolved fluid velocity seen by the particle. A general equation for a variable in a turbulent flow reads as follow:

$$u = \overline{u} + u', \tag{2.14}$$

in which the filtered term $\overline{u}$ represents the resolved fluid velocity seen by the particle and the fluctuating term u' denotes the unresolved fluid velocity.
With the aim to calculate the full fluid velocity seen by the particle, i.e. mean and fluctuating term , a *subgrid-scale (SGS) model* for particle is required to model the unresolved small scales of the fluid motion on the particle.
The calculation of the fluctuating term in the case of the particle motion is challenging due to the presence of two effects. First, the inertia of the particle induces a relative and instantaneous

displacement between particle and fluid particle. Second, the so-called crossing trajectories effect that, as Breuer et al. [6] explain in their paper, occurs when particles moves between vortexes.
In the literature there are several SGS models that are divided into 2 categories: approximate deconvolution models (ADM) and stochastic differential equations (SDE). Approximate deconvolution models are based on the idea to apply the reverse effect of the filtering process in order to recover the unresolved fluctuation and therefore provide the full fluid velocity. A shortcoming of the ADM method lies in the fact that in case of implicit LES, in which the filtering process is based on the length of the grid, it is not easy to apply the reverse function. The other category of SGS models is the Stochastic Differential Equation. They are also called *Langevin equations* and can provide the full fluid velocity seen by the particles (mean term plus fluctuating term), or only the unresolved one.
A general equation for this kind of model is

$$du_i' = A_i dt + B_{ij} dW_i, \tag{2.15}$$

where, in this case, it provides the derivative of the subgrid-scale velocity given by the sum of the drift term A_i multiplied by the timestep dt and the diffusion term $B_{ij}dW_i$. In this equation, the drift term leads the SGS velocity to an asymptotic values, while the diffusion term provides randomness, and therefore, the term dW denotes the increments of the Wiener process.

The aim of this work is to implement various SGS models and evaluate their performance. In the literature there are numerous SGS models, and those chosen for this study are explained below. They are divided into model for isotropic and anisotropic turbulence.

SGS model for isotropic turbulence

The SGS models developed for isotropic turbulence are divided into three different types of models. The first one includes the models in which the SGS term is added to the particle accelerations (Fukagata et al. [9]), i.e. in the RHS of the equation of motion. The second type are the models that add the SGS term to the fluid velocity seen by the particle (Jin et al. [14]). The third type includes the models that calculate the full fluid velocity seen (Shotorban et al. [24]).
Shotorban et al. [24] first developed an SGS model for a fluid particle and then applied the same formula to particles with inertia. Initially the differences from the previous equation were different Lagrangian time scale and coefficients of diffusion term. Those changes were due to the inertia effect that causes the particle to move in a different direction than the fluid particle. The shortcoming of this model arises from the assumption taken by Shotorban et al. [24], in

which the Lagrangian time scales and the coefficients of the diffusion term are the same for both cases because they are not able to calculate these values. For that reason, the model results slightly deviated from the DNS reference.
In contrast with Shotorban et al. [24], the stochastic model of Jin et al. [14] provides the full fluid velocity at the particle position. The main difference is the Lagrangian timescale. One of the simplest assumption about this timescale, noted by Shotorban et al. [24], is that the Lagrangian timescale is equal to the timescale for a fluid element, but this is true only for Stokes numbers $\ll 1$. For that reason, Jin et al. [14] proposed a Lagrangian timescale that depends on the Eulerian timescale and on the particle inertia through the Stokes number.
The model of Fukataga et al. [9] belongs to the first class of models, since it provides the SGS acceleration which is directly added on the RHS of the equation of motion. The most important characteristic of the Fukagata model is the range to which it is applied. This model works in the molecular range in which the particle size is small, and this leads to a short time step. For this reason, the Brownian motion must be taken into account.
The model of Wang et al. [1] is one of the simplest ones developed for isotropic turbulence in which the velocity fluctuation has no SGS temporal correlation, i.e. the fluctuating term does not depend on the time step. Rather, it considers the effects of the subgrid-scale velocity fluctuations on the particle statistics by solving a transport equation for the SGS kinetic energy k_{SGS}. Then, the SGS velocity fluctuation is obtained by sampling a random-number from a Gaussian probability density function (PDF) with zero mean and variance of $2k_{SGS}/3$.

SGS model for anisotropic turbulence

Several models can be found in the literature for anisotropic turbulence. The characteristic of this kind of turbulence is that the velocity fluctuations are different along the three axes and follow a preferential direction. In this case, there are stochastic models directly developed for the anisotropic turbulence (Berrouk et al. [4] and Innocenti et l. [13]) or models, that were created for the isotropic case and then extended to the anisotropic one, such as those of Bini et al. [5] and Amiri et al. [1].
The models of Berrouk et al. [4] and Innocenti et al. [13] are similar and provide the full fluid velocity at the particle position. Therefore, the drift term of both models consists of some terms that they take from the incompressible form of the Navier-Stokes equations. The drift and diffusion terms are closed with the filtered pressure and velocity fields as well as the residual kinetic energy and its dissipation rate. In order to predict the SGS fluctuation seen by the particles they take the particle inertia and the cross trajectory effect into account. Compared to Innocenti et al. [13], the model of Berrouk et al. [4] does not have spurious drift effects, such as stated byLain et al. [17], in the case of non-homogeneous turbulence the

conservation of the mass is guaranteed. The behaviour of the probability density functions is not assumed a priori for both models. In case of homogeneous turbulence the PDFs have a Gaussian distribution, while for non-homogeneous turbulence, the deviations from the Gaussian distribution are results of the modelling choices of the drift and diffusion terms.
The following two models are different from the previous ones because they were developed for isotropic turbulence and then modified to be used for anisotropic turbulence. The first is the model of Bini et al. [5] and consists solely of the diffusion part. This model adds the SGS term in the RHS of the equation of motion. If only the diagonal of the diffusion matrix is considered, a model for isotropic turbulence is obtained, while if we take all the components of the diffusion matrix into account, the model is valid for anisotropic turbulence. In this case, the PDF deviates strongly from the Gaussian distribution.
The second model is that of Amiri et al. [1] and is an extension of the model of Fukagata et al. [9], which is valid for isotropic turbulence only. In order to account for anisotropic turbulence, the fluctuation velocity from Fukagata et al. is multiplied by three different factors for each direction. These factors depend on the resolved fluid fluctuation u_i' and on the turbulent kinetic energy k_{SGS}.
In the following, two models have been chosen and implemented in order to evaluate their performance for the round-jet test case, both developed for anisotropic turbulence. The first is the stochastic model of Sommerfeld [17], which provides the fluctuation SGS velocity. The second is the the model of Minier et al. [19], which supplies the full fluid velocity at the particle position.
Afterwards, the model of Breuer et al. [6] is explained. This model was already implemented before the beginning of this work and its performance is evaluated and compared against the other models and the experimental results.

Sommerfeld Sommerfeld's [17] model involves a method based on the two-step (Lagrangian-Eulerian) approach. He applies this method due to the presence of the inertia of the particles and due to the mean drift, which cause a relative displacement between the particle and the fluid element surrounding it.

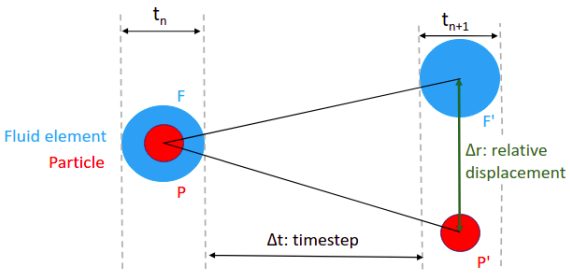

Figure 2.1: Solid and fluid particle trajectories

As you can see in Fig. 2.1, at time t_n the particle P and the fluid element F are in the same point, but due to inertia and mean drift, the solid particle is at the point P' at the next time t_{n+1}, whereas the fluid particle is at F'. Sommerfeld's idea involves a Lagrangian and an Eulerian step. In the first one the velocity of the same fluid particle at t_n and t_{n+1} is computed, while the second step is used to generate the new driving velocity from F' to P' at time t_{n+1}.
In the Sommerfeld model the shape of the PDF of the SGS velocity is assumed beforehand. This assumption leads to the conclusion that a Gaussian distribution of the PDF is present in the case of homogeneous turbulence, otherwise it is not present. Therefore, the form of the correlation function (see Eq. (2.17)) is also assumed a priori, and Sommerfeld develops a stochastic model following that form. One of the advantages of this model is that Sommerfeld, with the Euler-Lagrangian approach in the correlation function R_P, considers the crossing-trajectory effects. A shortcoming is that the model suffers from spurious drift effects.
The Sommerfeld model [17] is described by the following Langevin equation

$$u_i'^{n+1} = \underbrace{r_{P,i}(\Delta t,\Delta r)u_i'^{n}}_{drift-term} + \underbrace{\sigma_{fi}\sqrt{1-r_{P,i}^2(\Delta t,\Delta r)}dW_i}_{diffusion-term}, \qquad i = 1,2,3, \tag{2.16}$$

where the first term of Eq. (2.16) is the drift term and the second is the diffusion one. The term dW_i represents the increments of the Wiener process characterised by a Gaussian distribution with zero mean and variance equal to the timestep. The term σ_{fi} is the root mean square (rms) of the resolved fluctuations $\sqrt{\boldsymbol{u'^2}}$. The last term that appears in Eq. (2.16) is $r_{P,i}$, which is the correlation function that has Lagrangian and Eulerian components as explained in Fig. 2.1, given by

$$r_{P,i}(\Delta t,\Delta r) = r_{L,i}(\Delta t)R_{E,ii}(\Delta r), \tag{2.17}$$

where the double index ii denotes the trace of the matrix $\boldsymbol{R_E}$. The correlation function consist of two terms, $\boldsymbol{r_L}$ and $\boldsymbol{R_E}$, which are the Lagrangian and Eulerian component, respectively.
The Lagrangian correlation depends exponentially on the Lagrangian time scale $t_{L,i}$:

$$r_{L,i}(\Delta t) = exp\left(-\frac{\Delta t}{t_{L,i}}\right), \quad t_{L,i} = C_T\frac{\sigma_{fi}^2}{\epsilon}, \tag{2.18}$$

where Δt is the timestep and C_T a constant equal to 0.24. The Lagrangian time scale is a function of the resolved fluctuations $\boldsymbol{u'}$ and the energy dissipation rate ϵ. Following the idea of Shotorban et al. [24], the dissipation rate is approximated by

$$\epsilon = C_\epsilon\frac{k_{SGS}^{3/2}}{\Delta}, \tag{2.19}$$

where C_ϵ is a model constant equal to 19/12 according to Heinz [10] and Δ is the filter width.

In order to solve Eq. (2.19) the turbulent kinetic energy is estimated according to Bardina et al. [2] in which the fluid velocity field $\boldsymbol{u_f}$ is double-filtered:

$$k_{SGS} = \frac{1}{2}(\overline{\boldsymbol{u_f}} - \overline{\overline{\boldsymbol{u_f}}})^2. \tag{2.20}$$

When the turbulent kinetic energy is estimated, the energy dissipation rate ϵ can be approximated as well, and once the Lagrangian correlation function is calculated, the next step is the computation of the Eulerian correlation function. It depends on the relative displacement between the fluid element and the solid particle $\Delta r = |\boldsymbol{u^n} - \boldsymbol{u_p^n}|\Delta t$, where ^{n} denotes the current timestep. $\boldsymbol{R_E}$ is given by

$$R_{E,ij}(\Delta r) = [f(\Delta r) - g(\Delta r)]\frac{\Delta r_i \Delta r_j}{\Delta r^2} + g(\Delta r)\delta_{ij}, \tag{2.21}$$

where f and g are exponential functions, which depend on Δr as well and are given by

$$f(\Delta r) = exp\left(-\frac{\Delta r}{L_E}\right), \tag{2.22}$$

$$g(\Delta r) = \left(1 - \frac{\Delta r}{2L_E}\right) exp\left(-\frac{\Delta r}{L_E}\right). \tag{2.23}$$

L_E represents the scalar Eulerian timescale and is provided by

$$L_E = C_L t_{Lf} \sigma_f, \quad t_{Lf} = C_T \frac{\sigma_{fi}^2}{\epsilon}, \quad \sigma_f^2 = \frac{1}{3}\overline{u_i' u_i'}, \tag{2.24}$$

and depends on the model constant C_L. According to Lain et al. [17], C_L is set to 3.

Minier & Peirano The model of Minier et al. [17] is developed using the Navier-Stokes equations and provides the full fluid velocity at the particle position. In this model, the shape of the PDF of the fluid SGS velocity and the correlation functions are not assumed a priori, but are a result of the model. In case of homogeneous turbulence the PDF follows a Gaussian distribution, whereas for non-homogeneous turbulence the PDF is not Gaussian.
One of the advantages of Minier et al. [17] model is that it does not suffer from spurious drift effects. As Lain et al. [17] state, the model is not affected by those problems due to the presence of the mean pressure gradient in the drift term (Eq. (2.25)). Finally, this model also takes the crossing trajectories effects into account.
Initially, Minier et al. [17] considered the analogy with the Langevin equation for the SGS velocity of a fluid particle. To extend the model to a solid particle with inertia and take the crossing trajectory effects into account, they used a similar Langevin equation for the fluid

particle, but with some changes especially for the drift term. Due to the fact that the model provides the full subgrid-scale velocity, they mantein the idea of the decomposition into a mean and a fluctuating term. Based on the two-step approach of Sommerfeld [17], the model of Minier et al. [19] obtain the mean term from a first-order Taylor development for small dt. Minier et al. describe the model with the following Langevin equation

$$du_i = \underbrace{\left[-\frac{1}{\rho}\frac{\partial\langle p\rangle}{\partial x_i} + (\langle u_{p,j}\rangle - \langle u_{f,j}\rangle)\frac{\partial u_{f,i}}{\partial x_j} + G_{ij}(u_j - \langle u_j\rangle)\right]}_{A_i:drift-term} dt + \underbrace{B_{ij}dW_j}_{diffusion-term}, \tag{2.25}$$

where i,j = 1,2,3 and the $\langle\cdot\rangle$ represents the mean value interpolated to the particle position. The first two terms of the drift term, where the gradients appear, represent the *mean part*, whereas the other two terms denote the *fluctuating part*. In Eq. (2.25), the second term represents the velocity difference between the particle and the mean fluid velocity multiplied by the fluid velocity gradient.
The drift matrix $\boldsymbol{G}$ is given by

$$G_{ij} = -\frac{1}{T^*_{L,\perp}}\delta_{ij} - \left[\frac{1}{T^*_{L,||}} - \frac{1}{T^*_{L,\perp}}\right] r_i r_j, \tag{2.26}$$

which considers the cross-trajectory effect due to the presence of the two different Lagrangian time scales. In Eq. (2.26), r_i and r_j are the normalized relative velocities between particle and fluid $r_i = \langle u_{r,i}\rangle/|\langle \boldsymbol{u_r}\rangle|$, with $\langle \boldsymbol{u_r}\rangle = \langle \boldsymbol{u_p}\rangle - \langle \boldsymbol{u_f}\rangle$. Therefore, $T^*_{L,||}$ and $T^*_{L,\perp}$ are the Lagrangian time scales seen by the particles in the parallel and perpendicular directions to the mean drift, respectively. According to Csanady's analysis [7], the integral time scales of the fluid seen by the particle have to be different from the integral time scale of the fluid velocity due to crossing trajectory effects. The new Lagrangian time scales are given by

$$T^*_{L,||} = \frac{T_L}{\sqrt{1 + \beta^2\frac{|\langle \boldsymbol{u_r}\rangle|}{2k_{SGS}/3}}}, \quad T^*_{L,||} = \frac{T_L}{\sqrt{1 + 4\beta^2\frac{|\langle \boldsymbol{u_r},\rangle|}{2k_{SGS}/3}}} \tag{2.27}$$

where $\beta = T_L/T_E$ is the ratio between the Lagrangian and Eulerian fluid time scale and following the idea of Pozorski et al. [22] β is set to 1. Therefore, k_{SGS} is the turbulent kinetic energy of the subgrid-scales.
The fluid Lagrangian timescale is given by

$$T_L = \frac{4}{3(C_0 + 2/3)}\frac{k_{SGS}}{\epsilon}, \tag{2.28}$$

where C_0 is a models constant equal to 19/12 according to by Stephan Heinz [10]. The tubrulent kinetic energy k_{SGS} and its dissipation rate ϵ are calculated with Eq. 2.20 and 2.19, respectively. Defined the Lagrangian timescale with Eq. (2.28), Eq. (2.26) can be rewritten as follows

$$G_{ij} = -\left(\frac{1}{1} + \frac{3}{4}C_0\right)\frac{k_{SGS}}{\epsilon}H_{ij}, \tag{2.29}$$

where the matrix $\boldsymbol{H}$ considers the Csanady's analysis and is given by

$$H_{ij} = b_\perp \delta_{ij} + (b_{||} - b_\perp) r_i r_j, \tag{2.30}$$

where $b_{||} = T_L/T^*_{L,||}$ and $b_\perp = T_L/T^*_{L,\perp}$ are the Csanady's factors.
The closure of the diffusion term is calculated by a Cholewski decomposition:

$$B_{ij}B^T_{ij} = D_{ij}, \tag{2.31}$$

where $\boldsymbol{B^T}$ is the transpose of $\boldsymbol{B}$ and the symmetric matrix $\boldsymbol{D}$ reads as follow

$$D_{ij} = \epsilon\left(C_0\lambda H_{ij} + \frac{2}{3}(\lambda H_{ij} - \delta_{ij})\right). \tag{2.32}$$

In Eq. (2.32), the factor λ is

$$\lambda = \frac{3Tr(\boldsymbol{HR})}{2k_{SGS}Tr(\boldsymbol{H})}, \tag{2.33}$$

where $Tr(\cdot)$ denotes the trace and $\boldsymbol{R}$ is the fluid Reynolds stress tensor given by the resolved fluid fluctuations $R_{ij} = \overline{u'_i u'_j}$.

Breuer et al. The model of Breuer et al. [6] is based on the normalized model of Pozorski et al. [22]. The main assumption of Pozorski et al. [22] is that the direction of the relative velocity between particle and fluid is aligned with the main axes, along which the flow develops. To consider that the relative velocity can have any direction in the space, Breuer et al. [6] transform the drift and the diffusion terms of the model of Pozorski et al. [22] into matrices.
The model of Breuer et al. [6] is based on the following equation:

$$du'_i = \underbrace{-G_{ij}u'_j dt}_{drift-term} - \underbrace{\sqrt{2\sigma^2_{SGS}}B_{ij}dW_j}_{diffusion-term}, \tag{2.34}$$

where i,j = 1,2,3. On the left hand side, du'_i is the derivative of the SGS velocity. On the right hand side dt is the timestep and G_{ij} and B_{ij} are the drift and the diffusion matrices, respectively.

The term dW_j represents the increment of the Wiener process based on a Gaussian distribution with zero mean and variance equal to the timestep.
σ_{SGS} is the standard deviation of the SGS velocity and is given by

$$\sigma_{SGS} = \sqrt{\frac{2k_{SGS}}{3}}, \tag{2.35}$$

where k_{SGS} is the turbulent kinetic energy of the subgrid-scales estimated by Eq. (2.20) with the double-filtering process according to Bardina et al. [2].
The matrix $\boldsymbol{G}$ is the same as the the Minier et al. [17] model and is defined by Eq. (2.26), while the matrix B_{ij} reads as follow:

$$B_{ij} = -\frac{1}{\sqrt{T^*_{L,\perp}}}\delta_{ij} - \left[\frac{1}{\sqrt{T^*_{L,||}}} - \frac{1}{\sqrt{T^*_{L,\perp}}}\right] r_i r_j, \tag{2.36}$$

In Eq. (2.36), r_i and r_j are the normalized relative velocities between particle and fluid $r_i = \langle u_{r,i}\rangle / |\langle \boldsymbol{u_r}\rangle|$, where $\langle \boldsymbol{u_r}\rangle = \langle \boldsymbol{u_p}\rangle - \langle \boldsymbol{u_f}\rangle$.
$T^*_{L,||}$ and $T^*_{L,\perp}$ are calculated by Eq. (2.27) and represent the Lagrangian time scales seen by the particles in the parallel and perpendicular directions to relative velocity, respectively. In the model of Breuer et al. [6] the Lagrangian time scale T_L is approximated by

$$T_L = C\frac{\Delta}{\sigma_{SGS}}, \tag{2.37}$$

where C is a model constant and following the concept of Breuer et al. [6], is set to 1, while Δ is the filter width, i.e. the length of the grid in our case.

3 Simulation setup

This chapter presents an overview of the parameters used to evaluate the performance of the model of Sommerfeld [17], Minier et al. [17] and Breuer et al. [6] for the round-jet test case. In the first section how the models are validated in FLEXI is explained, then, the characteristics of the mesh, the particles and the fluid are described. Finally, the numerical methods employed for the simulations are presented.

3.1 Validation of the implementation

To investigate and compare the results of the subgrid-scale models, their FLEXI implementation has to be validated. The validation only considers the Sommerfeld [17] and Minier et al. [17] models because the Breuer et al. [6] model was already implemented in FLEXI and validated before the beginning of this work. For the validation, the SGS models are implemented in FLEXI and Python and then the SGS velocity and its path length provided by the two codes are compared.
The implementation of the SGS models, requires some information from the fluid phase (fluid fluctuations, density, fluid velocity) and from the mesh (grid length), but these are not available in Python. Thus, to compare the results with FLEXI, these variables are fixed.
Both models are based on a Langevin equations in which the Wiener process is described by a random variable from a Gaussian distribution. This means that the models are compared without considering the Wiener process, otherwise the SGS results would be different.
For the FLEXI validation, the test case used in order to run the code is a periodic box of 2π with a DOF of 32 in every direction and a polynomial degree N equal to 1. Then, only one particle is inserted in the computational domain. Finally, the simulations run for 5 seconds with the same timestep dt in both FLEXI and Python. Detailed information about the values used are shown in table 3.1.

For the model of Sommerfeld [17], in addition to the assumptions summarized in the table 3.1 the model requires the resolved fluid fluctuations in every direction and the velocity difference between particle and fluid. They are summarized in Table 3.2.

Parameters	Symbols	Values	Units
Timestep:	dt	$5 \cdot 10^{-3}$	[s]
Grid-length:	Δ	$2\pi/32$	$[m]$
Fluid density:	ρ_f	1	$[kg/m^3]$
Dynamic viscosity:	μ_0	$8.78151 \cdot 10^{-4}$.	$[Pa \cdot s]$
Particle diameter:	d_p	$8 \cdot 10^{-5}$	[m]
Particle density:	ρ_p	1814	$[kg/m^3]$

Table 3.1: Values used for the validation of the models of Sommerfeld and Minier et al.

Parameters	Symbols	Values	Units
Resolved fluid fluctuation:	$\overline{\boldsymbol{u}_i'}$	[0.1,0.1,0.1]	$[m/s]$
Relative velocity:	$\boldsymbol{u} - \boldsymbol{u_p}$	[1,1,1]	$[m/s]$

Table 3.2: Additional assumptions for Sommerfeld validation

The results of the SGS velocity and its path length are shown in Fig. 3.1 and in Fig. 3.2, respectively.

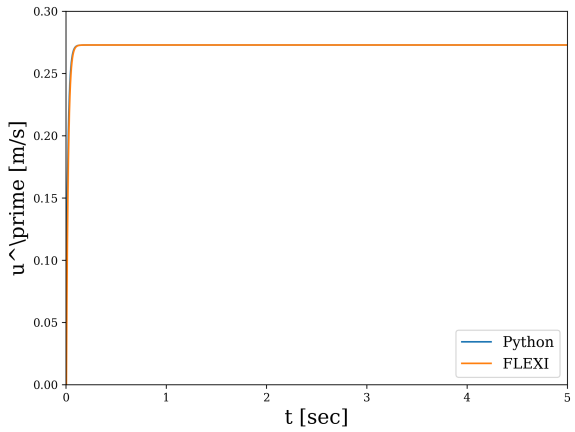

Figure 3.1: SGS velocity from Sommerfeld model

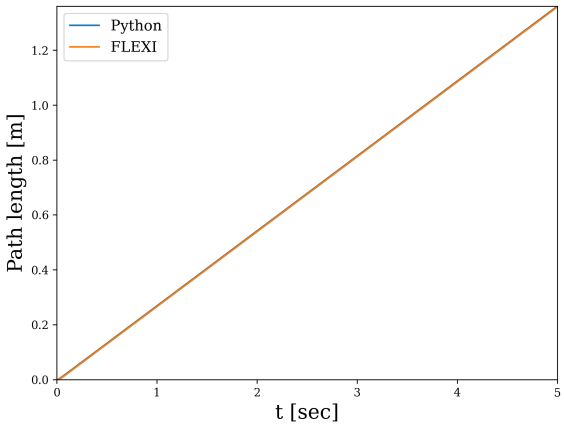

Figure 3.2: SGS path length from Sommerfeld

In both cases, the curves from FLEXI and Python coincide exactly for both fluctuation velocity and path length, which means that the implementation in FLEXI is validated. In Fig. 3.1 the fluctuation reaches the asymptotic value because the random part is not considered. In Fig. 3.2 the path length increases further and further because it is given by a simple integration of the velocity.

The validation of the model of Minier et al. [17] requires to fix more variables than Sommerfeld [17] because Minier et al. [17] provides the full fluid velocity seen by the the particle, and because some terms of the Navier-Stokes equation as the pressure and velocity gradients appear in the model. The assumptions are summarized in the Table 3.3.

Parameters	Symbols	Values	Units
Resolved fluid fluctuation:	$\overline{\boldsymbol{u_i'}}$	[0. 1,0. 1,0. 1]	$[m/s]$
Fluid velocity:	$\boldsymbol{u_i}(\boldsymbol{x}(t),t)$	[1,1,1]	$[m/s]$
Pressur gradient:	$\partial\langle p\rangle/\partial x_i$	[15,15,15]	$[Pa/m]$
Fluid velocity gradient:	$\partial u_i/\partial x_j$	1 (for each component of the matrix)	$[s^{-1}]$

Table 3.3: Additional assumptions for Minier et al. validation

The results of the SGS velocity and its path length are shown in Fig. 3.3 and in Fig. 3.4, respectively.

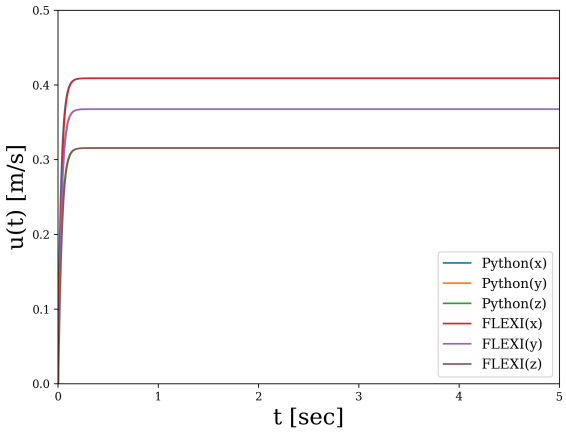

Figure 3.3: SGS velocity from Minier et al.

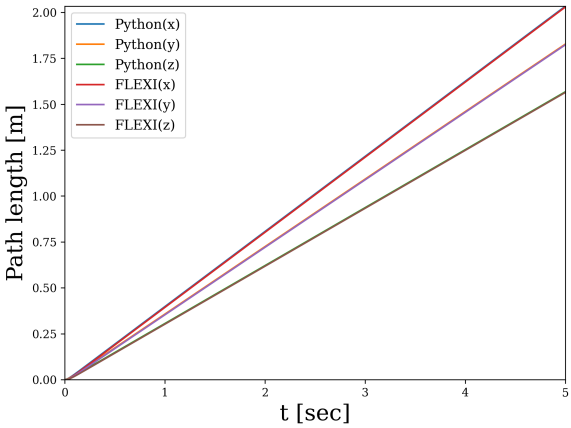

Figure 3.4: SGS path length from Minier et al.

The model of Minier et al. [17] provides three different velocities and path lengths for the three spatial directions. In addition, the SGS velocity provided by the model reaches an asymptotic values. In Fig. 3.3 and Fig. 3.4 the curves coincide perfectly for both Python and FLEXI, i.e. the implementation is validated.

3.2 Mesh Characteristics

To numerically represent the experiments of Fan et al. [8] and compare the SGS models the mesh of the round-jet is required. The mesh is shown in Fig. 3.5 and is built with HOPR [11], an open source high-order generator mesh, developed at the University of Stuttgart, in order to create 3-D high-order meshes.

The computational domain of the round-jet used for the simulation consists of two parts. The first one is the pipe that has the same diameter of Fan et al. [8] experiment $d_{pipe} = 4 \cdot 10^{-2} m$ and a length of $0.1\ m$ in the streamwise direction. The second part is the chamber where the particles spread out and is a cylindrical zone with radius of $0.11\ m$ and a length of $0.42\ m$.

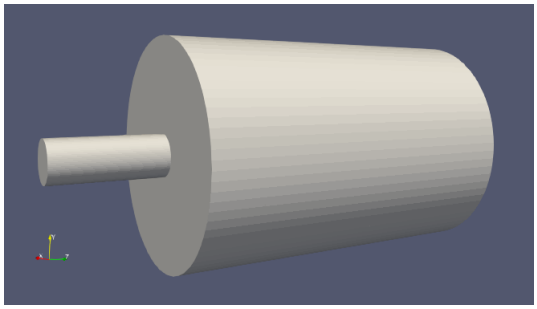

Figure 3.5: Round-jet

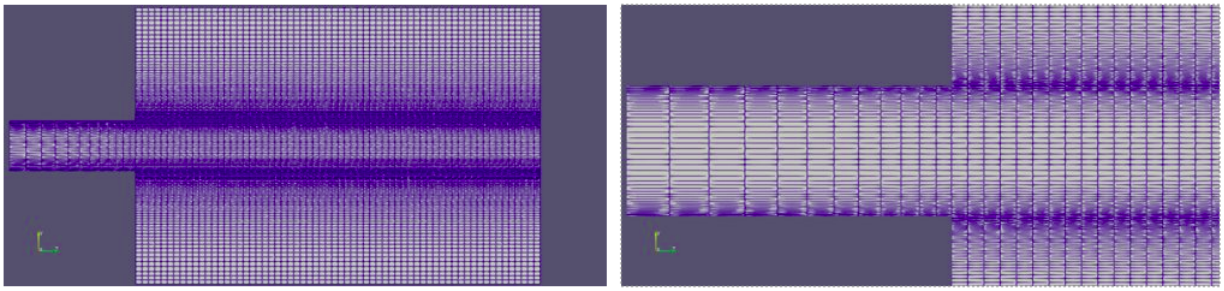

Figure 3.6: Cross sections of the round-jet

In the present work, the computational domain of the first part is resolved by 25x12 elements in radial and streamwise directions, respectively, while for the chamber 88x64 elements in radial and streamwise direction are used. FLEXI is a solver based on a DGSEM scheme, which means that each element is approximated by polynomials of degree N. For these simulations $N = 4$ is set and it leads to $1.44975 \cdot 10^7$ degrees of freedom. In the pipe for the wall resolution a $y^+ = 3$ is used that leads to a height of the first cell y $= 2.2 \cdot 10^{-4} m$. The same y^+ is used for the chamber to analyze the shear layer zone, which considers the spreading rate S of the round-jet. In this work, S is set to 0.1 according to Pope [21]. In Fig. 3.6 two cross sections to visualize the elements of the mesh are portrayed. The picture on the right side includes a zoom of this mesh between pipe and chamber.
The initial conditions set in the pipe are the centerline velocity and the laminar blasius boundary layer $\delta_{99} = 1 \cdot 10^{-3} m$, while the fluid is at rest in the main chamber. The boundary conditions chosen are adiabatic walls for the pipe, free-stream outlet for walls of the chamber and pressure outlet for the outflow with a value of 101325 Pa.

3.3 Continuous and dispersed phase characteristics

To evaluate the performance of subgrid-scale models for the round-jet, the same setup of the experiment of Fan et al. [8] is set. The Reynolds number based on the initial centerline velocity and on the diameter of the pipe is 53571. The flow and particle characteristics are summarized

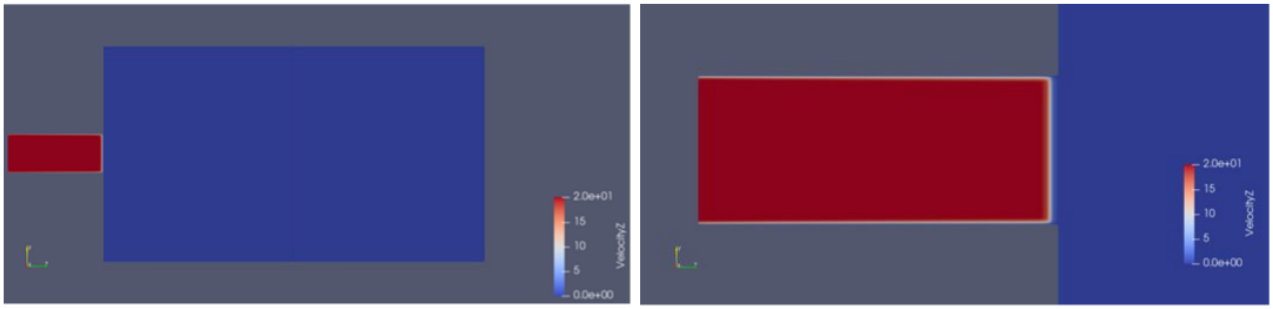

Figure 3.7: Initial conditions (axial velocity)

Parameters	Symbols	Values	Units
Continuous phase			
Centerline velocity	$\boldsymbol{u_0}$	20	$[m/s]$
Density	ρ_f	1.178	$[Kg/m^3]$
Dynamic viscosity	μ_0	$1.75916 \cdot 10^{-5}$	$[Pa \cdot m]$
Particle phase			
Centerline velocity	$\boldsymbol{u_{p,0}}$	19.1	$[m/s]$
Density	ρ_p	1250	$[Kg/m^3]$

Table 3.4: Conditions for continuous and dispersed phase

in Tab. 3.4.

After the flow validation, 250 particles, with a fixed centerline axial velocity, are emitted in the fluid every $1 \cdot 10^{-3}$ seconds for 2 flow-through times. They are randomly inserted at the beginning of the pipe in a disc-shaped of the same radius as the pipe where the particles are uniformly distributed. In the experiment Fan et al. [8], the non-uniform distribution portrayed in Fig. 3.8 is used, in which there are 11 species with different diameters. The relative values of the particle relaxation time τ_p and Stokes number St based on the initial fluid centerline velocity and the pipe diameter are summarized in Table 3.5. To compare the result with the experimental data of Fan et al. [8], the distribution has to be followed as well. In the present work only the 1-way coupling is considered, which means that the bins are independent from each other because particle-fluid and particle-particle interactions are not considered. Therefore, to obtain statistically correct results, a minimum number of particles that does not depend on the diameters is required. This means that the same number of particles can be set for all the diameters, i.e. uniform distribution. Then, to obtain the distribution of the experiment again, the uniform distribution is re-scaled simply by multiply each bin with the corresponding probability of Fan et al. [8]. The benefit of this approach is to save computational time. In fact, the use of a non-uniform distribution requires a higher number of particles for the highest bins, i.e. more computational, but the results would be statistically the same.

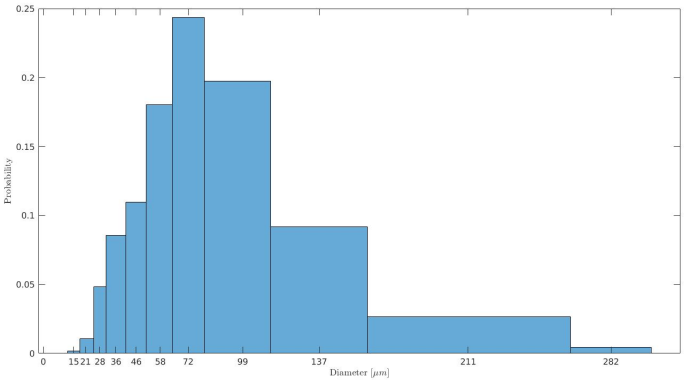

Figure 3.8: Particle diameter distribution

Species	Diameter	Particle relaxation time	Stokes number
	ρ_p	τ_p	St
	$[\mu m]$	$[s]$	[-]
Species 1	15	$8.88 \cdot 10^{-4}$	0.31
Species 2	21	$1.74 \cdot 10^{-3}$	0.87
Species 3	28	$3.09 \cdot 10^{-3}$	1.55
Species 4	36	$5.12 \cdot 10^{-3}$	2.55
Species 5	46	$8.35 \cdot 10^{-3}$	4.18
Species 6	58	$1.33 \cdot 10^{-2}$	6.64
Species 7	72	$2.05 \cdot 10^{-2}$	10.23
Species 8	99	$3.87 \cdot 10^{-2}$	19.35
Species 9	137	$7.41 \cdot 10^{-2}$	37.05
Species 10	211	$1.76 \cdot 10^{-1}$	87.88
Species 11	282	$3.14 \cdot 10^{-1}$	156.96

Table 3.5: Characteristics of the particle species used in the simulations

3.4 Numerical methods

To solve the equations, two different methods are used in this work. First, a high order low-storage Runge-Kutta method is used for the time integration of the Navier-Stokes equations. Second, for the integration of the SGS models it is not possible use the same method due to the presence of the Wiener process that is time-independent. Thus, the SGS models are integrated in time with an explicit Euler–Maruyama scheme according to Kloeden et al. [15].

4 Results and discussion

In this chapter, the performance of the three SGS models, Sommerfeld et al. [17], Minier et al. [17] and Breuer et al. [6] are evaluated. The results of those models are compared with a simulation in which no SGS model is applied and with the experimental data of Fan et al. [8]. All the data are plotted over the jet radius, r/r_0, where r is the local distance from the centerline and r_0 is the radius of the pipe. Therefore, all the results are plotted for different distances (planes) from the inlet of the jet z/d_p, where z is the distance in meters and d_p is the diameter of the pipe.

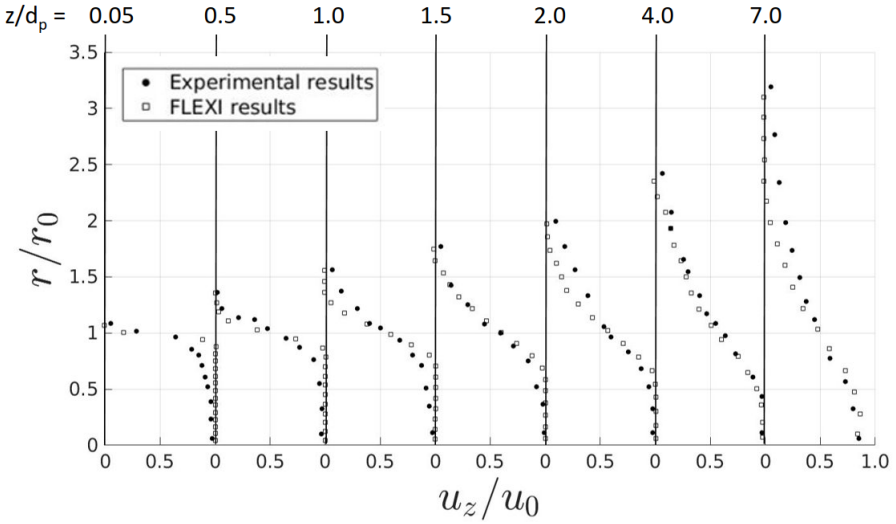

Figure 4.1: Radial profiles of gas phase mean axial velocity

Before the evaluation the SGS models for particles, the flow field has to be validated. Fig. 4.1 displays the mean gas phase axial velocity of the numerical simulations compared with that of the experiment of Fan et al. [8]. The mean radial velocity profiles appears in a dimensionless form, i.e. normalized by the initial jet center-line velocity u_0. The results of the simulation are in good agreement with the experimental data. For this validation the fluid ran for 0.050 seconds which means around 2,5 flow-through times. In order to obtain the results portrayed in Fig. 4.1 the time averaging is applied to the state files of FLEXI and a screenshot of the

time averaged states is displayed in Fig. 4.2. Therefore, in Fig. 4.3 the axial flow velocity of the last state file used for the flow validation is displayed.

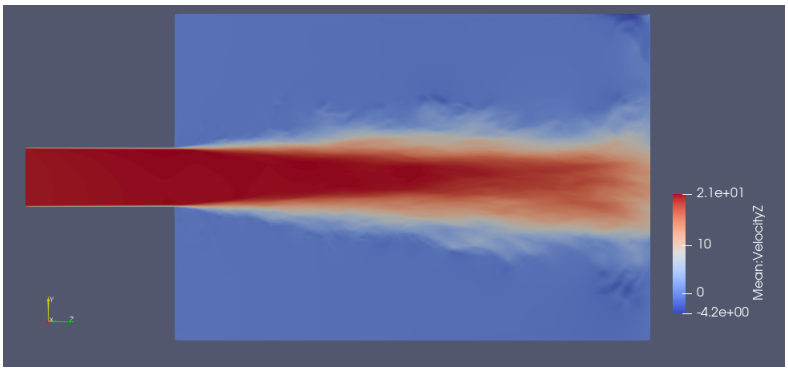

Figure 4.2: Time average of axial flow velocity in a cross section of the round-jet

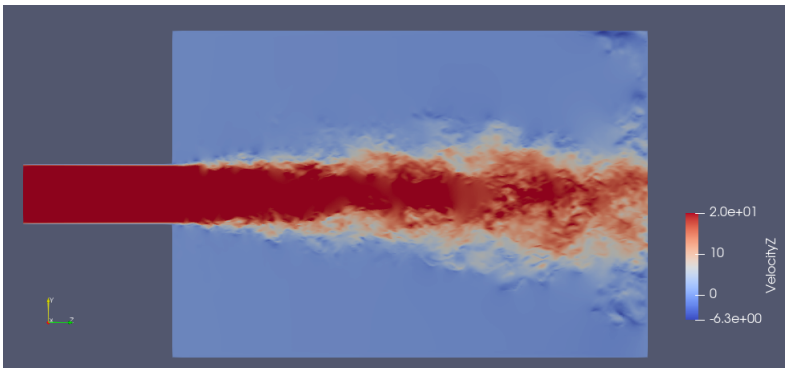

Figure 4.3: Last instantaneous of flow axial velocity

Despite the fact that fluid moves on for 2,5 flow-through times and the axial flow velocity is similar to that of Fan et al. [8], the boundary conditions influence the flow and the results as well. In fig. 4.4 the time averaged mean axial fluid fluctuations in a cross section of the round-jet are represented. Due to the boundary conditions the jet does not reach a totally stationary state, which means no convergence in a statistical sense. This introduces an error on the results.

4.1 Comparison again experimental results

In this section, the numerical results are compared to the experimental data of Fan et al. [8]. Fig. 4.5 shows the mean axial particle velocity u_{p_z} for each simulation (Sommerfeld et al. [17], Minier et al. [17], Breuer et al. [6], no SGS model) and for Fan et al. u_{p_z} is plotted in a dimensionless form, i.e. normalized by the local mean axial velocity at the centerline u_{p_0}. The numerical results of all the simulations have the same trend of the experimental data and there

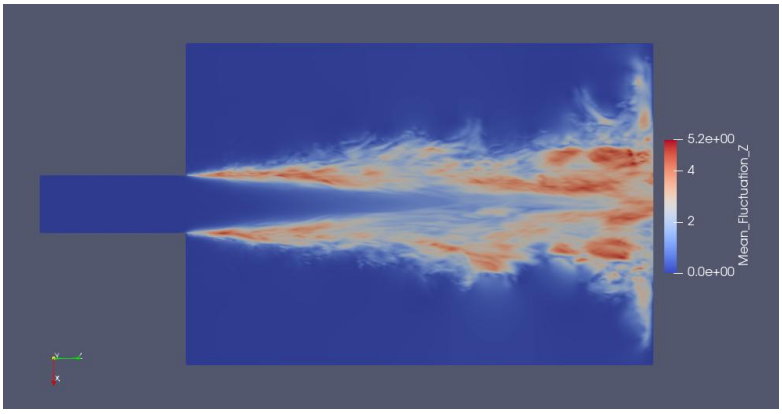

Figure 4.4: Mean fluid axial fluctuations

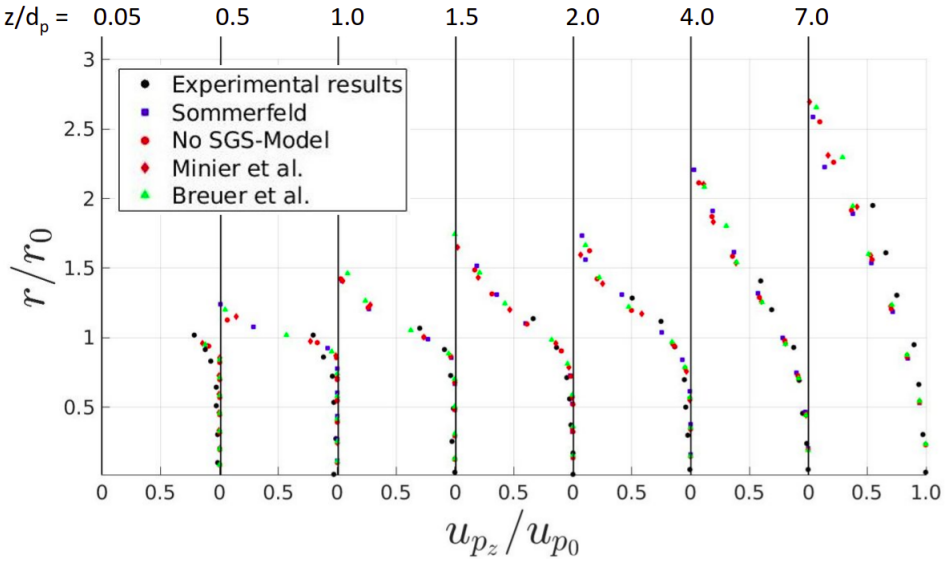

Figure 4.5: Radial profiles of mean particle axial velocity

are only small differences between the models. Except for the first plane, the particle spreading is higher than that of experimental results for each simulation. Fig. 4.6 displayed the spreading of the flow and of the particles for both cases, simulations and experiment results. In this chart, the bins of the particle spreading of the numerical results are plotted as the mean of all four simulations. Detailed information about the spreading of each model and a comparison between them are given in the next section.

Fig. 4.6 shows that the spreading of the flow is quite equal in both cases (LES and experiment), while the spreading of the particles is higher in the numerical simulations. This behaviour can be attributed to the emission type of particles in the pipe. The particles are randomly emitted based on an uniform distribution. This, compared with the experiment of Fan et al. [8], led to more particles outside of the core of the jet, i.e. more spreading.

This theory is confirmed by the mean concentration of particle C over the jet radius plotted in Fig. 4.7. This quantity is normalized by the local centerline mean value C_0. Fig. 4.7 shows

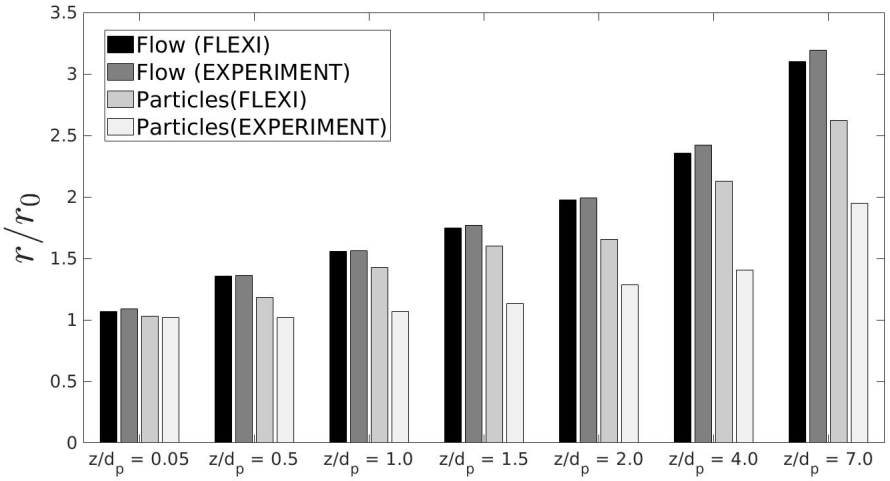

Figure 4.6: Spreading of the flow and of the particles

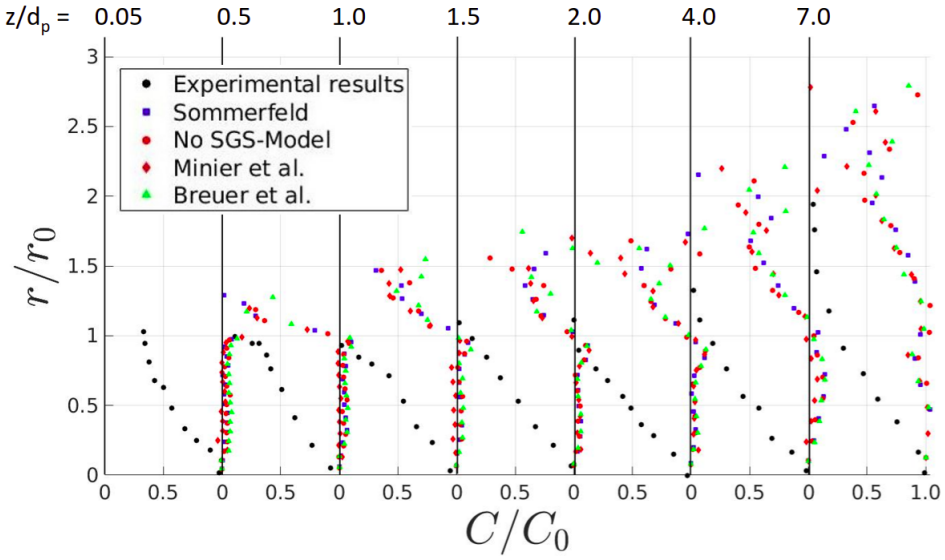

Figure 4.7: Radial profiles of mean particle concentration

that in the experimental data the concentration decreases as it moves away from the centerline, while for the numerical results, it is clear that due to the uniform distribution, the concentration in the core of the jet ($r/r_0 < 1$) is quite constant. Then, after that point, the particle concentration decreases.

The last quantity used to compare LES results with the experimental data of Fan et al. [8] is the mean particle axial turbulent kinetic energy (TKE). $\sqrt{u'_{p_z}{}^2}$ is plotted in Fig. 4.8 in a dimensionless form, i.e. divided by the local particle mean velocity. At the first plane, Fig. 4.8 shows that the turbulent kinetic energy is equal to 0 in the core region and in good agreement with Fan et al. [8] only in the region where $r/r_0 = 1$. Then, as we move forward, the TKE increases in the core of the jet as well. This behaviour is explained by the mean fluid axial

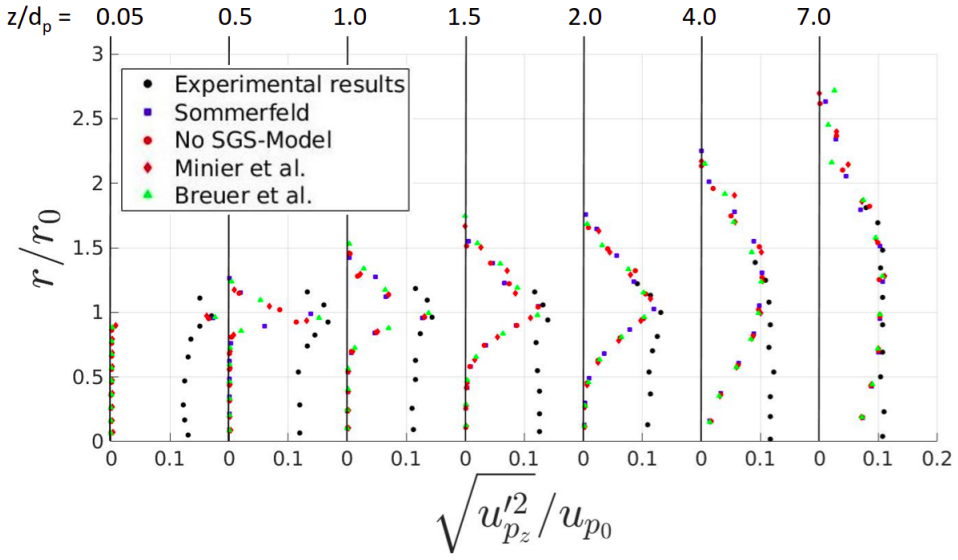

Figure 4.8: Radial profiles of mean particle axial turbulent kinetic energy

turbulent kinetic energy ($\sqrt{u_z'^2}$), in fact the particle TKE follows the same trend of the fluid TKE.

In Fig. 4.9, the comparison of the mean fluid axial TKE of the LES and that of the experiment of Fan et al [8] is plotted. The figure shows that the fluid TKE of the experiment is almost always greater than that of the simulations , except in $r/r_0 = 1$ region, where it increases in the simulations. Therefore, the fluid TKE of the LES is 0 in the core region, mostly at the beginning of the jet, and only in the last two planes the simulation results are in good agreement with the experiment.

These differences between simulations and experiment lay on the different boundary layer of the pipe. In the experiment of Fan et al. [8] at the round-jet inlet there is a fully developed turbulent pipe flow, which means that the flow is already turbulent in the core at the beginning of the round-jet as well. Instead, in FLEXI, a laminar boundary layer is set as initial condition and it remains laminar in the pipe, thus the turbulence develops further in the jet. For these reasons, the particle TKE of the numerical results displayed in Fig. 4.8 is 0 in the core regions and always lower than the TKE of Fan et al. [8]. Again for the same explanation, only in the last plane the two particle TKEs are in good agreement.

Then, in all the simulations, the maximum value of the particle TKE, in the experiment at $r/r_0 = 1$, is reached and after that point the simulations follow the same trend of Fan et al. [8]. Finally, Fig. 4.8 denotes that between the simulations in which the three SGS models are applied and that with no model there are only fewer differences.

From the comparison between simulations and experiment results shown in Fig. 4.5, Fig. 4.7 and Fig. 4.8, it appears that there are no differences between the SGS models and the case

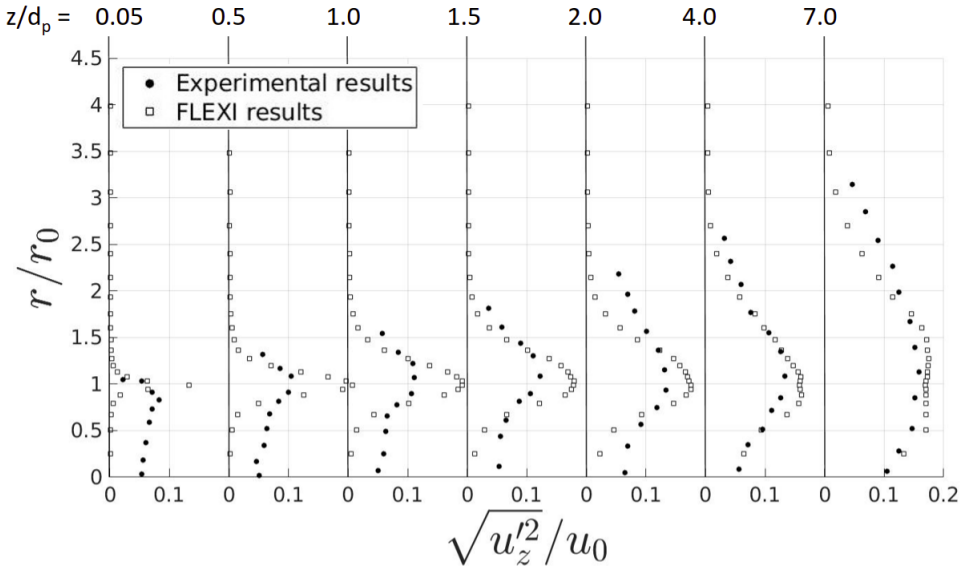

Figure 4.9: Radial profiles of mean fluid axial turbulent kinetic energy

without model. To better evaluate the performance of these models, further comparisons are analysed in the following section.

4.2 SGS models comparison

The comparison of the mean particle axial velocity shown in Fig. 4.5 highlights that the spreading in the numerical simulations is higher than that of the experiment of Fan et al. [8]. To analyse the particles behaviour with different SGS models Fig. 4.10 displays the spreading over the jet radius for the four simulations. First, Fig. 4.10 shows that the SGS models provide

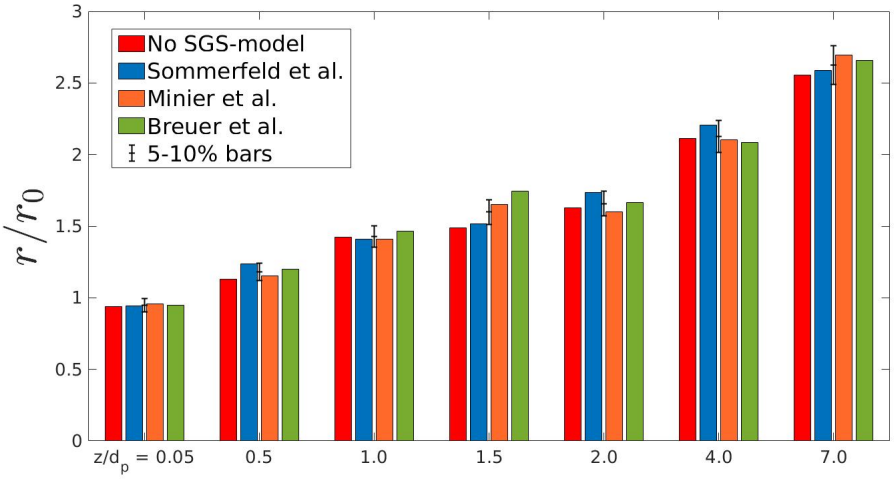

Figure 4.10: Spreading of particles for different SGS models and with no model

similar particle spreading for each plane. For instance, in the last plane the model with more spreading is Minier et al. [17], while in the other planes are the models of Sommerfeld [17] or Breuer et al. [6]. Second, even if it is not valid for every plane, the trend is that the case without SGS model leads to less spreading compared to those with SGS models. This is because the SGS velocity depends on a Gaussian distribution with zero mean, but with a variance greater than 0. This leads the velocity to deviate from the mean value, i.e. particles spread out more, while with no SGS model where the SGS fluctuations are not calculated the spreading is smaller.

Fig. 4.10 also shown that the spreading of the simulations deviates by a maximum of 5% from the mean spreading. This means that the biggest error between the simulation with the smallest spreading (in most cases without SGS model) and simulations with the highest spreading (mostly with SGS model) is of 10%. In conclusion, the difference between the three SGS models in terms of spreading is less than 10%.

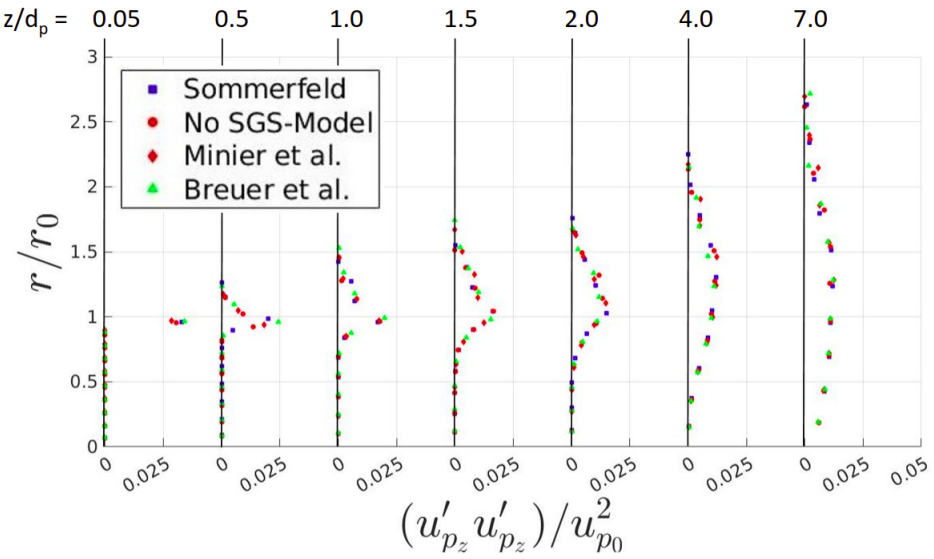

Figure 4.11: Mean variance of particle axial fluctuations

Fig. 4.11 shows the mean variance $u'_{p_z}u'_{p_z}$ for all the simulations, plotted in dimensionless form (divided by the square local particle axial velocity). The variance has the same trend of the turbulent kinetic energy and it is almost the same for each SGS model. For both Fig. 4.8 and Fig. 4.11, the results of the case without SGS model are similar to those in which the SGS models are applied. This is due to the fact that the fluid did not reach a completely stationary state, i.e. it is harder to compare the capability of the SGS models. Regardless, from this comparison it is possible to conclude that between the SGS model there are still no differences.

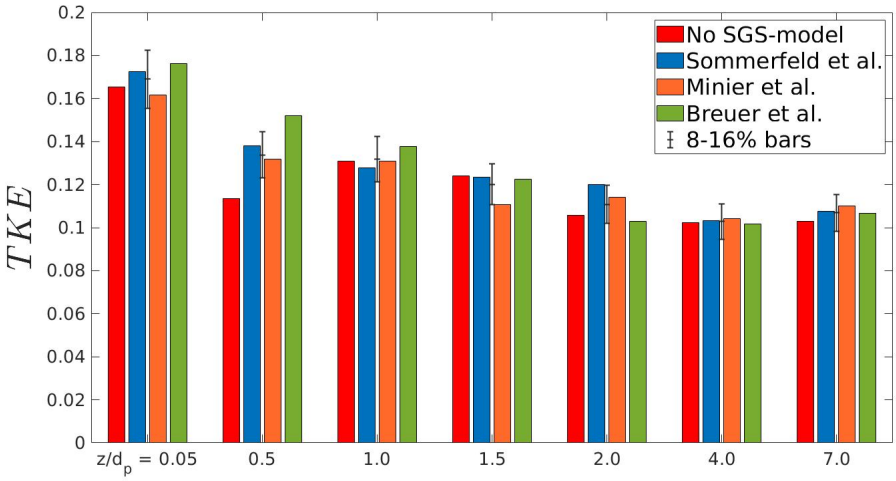

Figure 4.12: Axial TKE in the region $r/r_0 \approx 1$

Fig. 4.8 and Fig. 4.9 highlight that both fluid and particle fluctuations are comparable with the experimental results and have the highest values in the region $r/r_0 \approx 1$. For this zone, the maximum value of the particle TKE is plotted in Fig. 4.12 for each simulation and for different planes. The figure shows that the results of all simulations deviate from the mean value by 8%, i. e. the values differ from each other by a maximum of 16%.
This difference does not concern a specific model because there is not one that reaches the highest or smallest value in every plane. Therefore, the results of the simulation without the SGS model are in the same range as those where the model is applied. In conclusion, in terms of particle turbulent kinetic energy, there are no differences in the application or not of an SGS model.

5 Conclusion and outlook

The aim of this work was to analyse the performance of the SGS models of Sommerfeld [17], Minier et al. [17] and Breuer et al. [6] for a turbulent particle-laden flow in a round-jet flow. The Eulerian-Lagrangian approach was used in order to solve the turbulent multiphase flow numerically. Initially, the fluid phase was solved with the compressible form of the Navier-Stokes equations with the solver FLEXI [12]. The solution of the equations was obtained with an implicit LES, in which the scales smaller than the grid were unresolved. On the other hand, following the concept of Vinkovic et al. [25], a simplified equation of motion [23] was considered. The models of Sommerfeld [17] and Minier et al. [17] are both based on the same method (the Lagrangian-Eulerian two-step approach) to consider the particle inertia that produces relative displacement between the fluid and the particle. Therefore, all the three models take the crossing trajectory effects into account, but only the model of Minier et al. [17] did not suffer from spurious drift effects.

The numerical results were compared with the simulation without SGS model and with the experimental data of Fan et al. [8]. The comparison of the results with the experiment highlighted some differences in the quantities analysed. First, the particle axial velocity, even if it had the same trend of the experimental one for every simulation, presented a greater spreading in the simulations. This behaviour is due to the emission type (uniform) of the particle in the pipe and this is confirmed by the concentration. In the numerical simulations, where the particles were distributed uniformly, the concentration was constant in the core region, i.e. more particles were able to spread out of the core, while, in the experiment, the concentration already decreased from the centerline, i.e. less particles spread out.

The other difference with the experiment concerned the particle axial turbulent kinetic energy. The particle TKE provided by all the simulations was always smaller than the experimental one and reached similar values only in the region close to $r/r_0 = 1$. Similar results were obtained for the fluid TKE. In this case, there were these differences due to the fact that the flow in the pipe was at different conditions. In the experiment of Fan et al. [8], the pipe was fully developed turbulent, i.e. the turbulence was already in the core of the pipe at the jet inlet. In the simulation, the choice to set a blasius boundary layer led to a laminar flow in the pipe, i.e. the turbulence started only with the spreading of the flow in the round-jet due to the fact that

the boundary layer remains laminar in the pipe.
The comparisons between the LES result and the experiment of Fan et al. [8] denoted that all the simulations differed from the experiment, but the SGS models behaved similarly. To compare the single performance of the models, the spreading for each SGS model and for the case without it was analysed. It was determined that the SGS models provide similar particle spreading and that the trend was that the case without SGS model had less spreading. However, the difference between the simulations was less than 10%. The mean variance of the axial fluctuations was analysed as well and the results led to the same conclusion for the particle TKE, i.e. no differences between the models. Finally, the focus was on the area where fluctuations were at its greatest, with values similar to those of Fan et al. [8] ($r/r_0 \approx 1$). In that zone, the particle TKE provided by the simulations was again quite similar. For this case no simulation always reached the highest or the smallest value and the results differed from each other by a maximum of 16%.
In cocnclusion, the simulations differs from the experiment for two reasons. The first is in relation how the particles are emitted. For this case, a Gaussian distribution should be used to have more particles in the inner region of the core. With this correction it is possible to correctly represent the experimental data and obtain similar results for the spreading and the concentration. The second reason is related to the turbulence in the core. To achieve a fully developed turbulent pipe, as in the experiment of Fan et al. [8], the pipe of the round-jet should be longer to have the time to develop a turbulent boundary layer and to provide more turbulence, mostly in the core region and at the beginning of the round-jet.
Finally, from these simulations, only minor differences between the SGS models are visible, in which the variation of the results was between 10-16% in terms of spreading and particle TKE. In the end, to better evaluate the performance of these SGS models would be better to run different test cases.

Bibliography

[1] Amiri, A. E.; Hannani, S. K.; Mashayek, F.: *Large-eddy simulation of heavy-particle transport in turbulent channel flow.* Numerical Heat Transfer, Part B: Fundamentals, Bd. 50, Nr. 4, S. 285–313, 2006.

[2] Bardina, J.; Ferziger, J.; Reynolds, W.: *Improved subgrid-scale models for large-eddy simulation.* In: *13th fluid and plasmadynamics conference*, S. 1357. 1980.

[3] Beck, A.; Ortwein, P.; Kopper, P.; et al.: *Towards high-fidelity erosion prediction: On time-accurate particle tracking in turbomachinery.* International Journal of Heat and Fluid Flow, Bd. 79, S. 108457, 2019.

[4] Berrouk, A.; Laurence, D.; Riley, J.; et al.: *Stochastic modelling of inertial particle dispersion by subgrid motion for LES of high Reynolds number pipe flow.* Journal of Turbulence, , Nr. 8, S. N50, 2007.

[5] Bini, M.; Jones, W.: *Large-eddy simulation of particle-laden turbulent flows.* 2008.

[6] Breuer, M.; Hoppe, F.: *Influence of a cost–efficient Langevin subgrid-scale model on the dispersed phase of large–eddy simulations of turbulent bubble–laden and particle–laden flows.* International Journal of Multiphase Flow, Bd. 89, S. 23–44, 2017. URL: `https://www.sciencedirect.com/science/article/pii/S0301932215302123`.

[7] Csanady, G.: *Turbulent diffusion of heavy particles in the atmosphere.* Journal of Atmospheric Sciences, Bd. 20, Nr. 3, S. 201–208, 1963.

[8] Fan, J.; Zhang, X.; Chen, L.; et al.: *New stochastic particle dispersion modeling of a turbulent particle-laden round jet.* Chemical Engineering Journal, Bd. 66, Nr. 3, S. 207–215, 1997.

[9] Fukagata, K.; Zahrai, S.; Bark, F. H.: *Dynamics of Brownian particles in a turbulent channel flow.* Heat and mass transfer, Bd. 40, Nr. 9, S. 715–726, 2004.

[10] Heinz, S.: *On Fokker–Planck equations for turbulent reacting flows. Part 2. Filter density function for large eddy simulation.* Flow, Turbulence and Combustion, Bd. 70, Nr. 1, S. 153–181, 2003.

[11] Hindenlang, F.; Bolemann, T.; Munz, C.-D.: *Mesh Curving Techniques for High Order Discontinuous Galerkin Simulations.* In: *IDIHOM: Industrialization of High-Order Methods-A Top-Down Approach*, S. 133–152. Springer, 2015.

[12] Hindenlang, F.; Gassner, G. J.; Altmann, C.; et al.: *Explicit discontinuous Galerkin methods for unsteady problems.* Computers & Fluids, Bd. 61, S. 86–93, 2012.

[13] Innocenti, A.; Marchioli, C.; Chibbaro, S.: *Lagrangian filtered density function for LES-based stochastic modelling of turbulent particle-laden flows.* Physics of Fluids, Bd. 28, Nr. 11, S. 115106, 2016.

[14] Jin, G.; He, G.-W.; Wang, L.-P.; et al.: *Subgrid scale fluid velocity timescales seen by inertial particles in large-eddy simulation of particle-laden turbulence.* International journal of multiphase flow, Bd. 36, Nr. 5, S. 432–437, 2010.

[15] Kloeden, P. E.; Platen, E.: *Stochastic differential equations.* In: *Numerical Solution of Stochastic Differential Equations*, S. 103–160. Springer, 1992.

[16] Krais, N.; Beck, A.; Bolemann, T.; et al.: *FLEXI: A high order discontinuous Galerkin framework for hyperbolic–parabolic conservation laws.* Computers & Mathematics with Applications, Bd. 81, S. 186–219, 2021.

[17] Laín, S.; Grillo, C.: *Evaluation of Lagrangian particle dispersion models in turbulent flows.* Chemical Engineering Communications, Bd. 195, Nr. 3, S. 189–208, 2007.

[18] Maxey, M. R.; Riley, J. J.: *Equation of motion for a small rigid sphere in a nonuniform flow.* The Physics of Fluids, Bd. 26, Nr. 4, S. 883–889, 1983.

[19] Minier, J.-P.; Peirano, E.: *The pdf approach to turbulent polydispersed two-phase flows.* Physics reports, Bd. 352, Nr. 1-3, S. 1–214, 2001.

[20] Pelanti, M.; Quartapelle, L.; Vigevano, L.: *A review of entropy fixes as applied to Roe's linearization.* Teaching material of the Aerospace and Aeronautics Department of Politecnico di Milano, 2001.

[21] Pope, S. B.: *Turbulent flows*, 2001.

[22] Pozorski, J.; Apte, S. V.: *Filtered particle tracking in isotropic turbulence and stochastic modeling of subgrid-scale dispersion.* International Journal of Multiphase Flow, Bd. 35, Nr. 2, S. 118–128, 2009.

[23] Schwarz, A.; Kopper, P.; Kurz, M.; et al.: *An integrated high-order framework for multi-stage turbomachinery simulations.* In: *14th World Congress on Computational Mechanics (WCCM) & ECCOMAS Congress 2020.* Paris, France, Juli 2020.

[24] Shotorban, B.; Mashayek, F.: *A stochastic model for particle motion in large-eddy simulation.* Journal of Turbulence, , Nr. 7, S. N18, 2006.

[25] Vinkovic, I.; Aguirre, C.; Ayrault, M.; et al.: *Large-eddy simulation of the dispersion of solid particles in a turbulent boundary layer.* Boundary-layer meteorology, Bd. 121, Nr. 2, S. 283–311, 2006.